PEROVSKITES

Lead halide perovskites: Crystal-liquid duality, phonon glass electron crystals, and large polaron formation

Kiyoshi Miyata, Timothy L. Atallah, X.-Y. Zhu*

Lead halide perovskites have been demonstrated as high performance materials in solar cells and light-emitting devices. These materials are characterized by coherent band transport expected from crystalline semiconductors, but dielectric responses and phonon dynamics typical of liquids. This "crystal-liquid" duality implies that lead halide perovskites belong to phonon glass electron crystals, a class of materials believed to make the most efficient thermoelectrics. We show that the crystal-liquid duality and the resulting dielectric response are responsible for large polaron formation and screening of charge carriers, leading to defect tolerance, moderate charge carrier mobility, and radiative recombination properties. Large polaron formation, along with the phonon glass character, may also explain the marked reduction in hot carrier cooling rates in these materials.

INTRODUCTION: THE CRYSTAL-LIQUID DUALITY

Lead halide perovskites have emerged as superstars among materials for photovoltaics and light emission (*1*–*6*). A large number of studies have explored the mechanistic origins of their electronic properties, such as long carrier lifetimes, long carrier diffusion lengths, and exceptional defect tolerance (*7*–*11*). The unique properties of both hybrid organic-inorganic lead halide perovskites (HOIPs) and their all-inorganic counterparts result from the framework-like structure consisting of a sublattice of corner-sharing PbX_6^{3-} (X = I, Br, or Cl) octahedral with overall stoichiometry PbX_3^- and a sublattice of A^+ cations in the cuboctahedral voids, as shown schematically in Fig. 1 (*12*). Here, $A^+ = Cs^+$, Rb^+, $CH_3NH_3^+$ (MA), or $NH_2(CH)NH_2^+$ (FA). The framework structure leads to intrinsic softness and dynamic disorder. The former is shown by their Young's moduli being approximately 10× lower than those of Si or GaAs (*13*, *14*). The latter is reflected by broadening and anharmonicity in far-infrared (IR) and low-frequency Raman spectra, disorder in nuclear magnetic resonance (NMR) spectra and x-ray or neutron scattering, and liquid-like responses in dielectric function or femto- to picosecond responses (*15*–*26*).

For each lead halide perovskite, there are three main structural phases. In the low-temperature orthorhombic phase (T < 144.5 K and 370 K for $MAPbBr_3$ and $CsPbBr_3$, respectively), the $PbBr_6^{3-}$ octahedron undergoes Jahn-Teller distortion and the cation motion is restricted (*24*, *27*, *28*). For $MAPbBr_3$ ($CsPbBr_3$), the perovskite structure transitions to the tetragonal phase at T = 149.5 to 237 K (370 to 420 K) and the cubic phase at T > 237 K (420 K) (*24*, *27*, *28*). Similar phase transitions are present in I- and Cl-based perovskites. These transitions are accompanied by increasing dynamic disorder, particularly the orientational motions of organic cations in HOIPs (*26*).

The coexistence of a crystalline-like response in coherent band transport of charge carriers and a liquid-like response in phonon activities has prompted Zhu *et al.* (*25*) to call HOIPs "crystalline liquids" for the cubic and tetragonal phases. We can view the sublattice of organic cations as a confined liquid, with each polar molecular cation confined in a nanoscopic pore; thus, an HOIP in the high-temperature cubic phase is similar to a plastic crystal (*29*), which refers to a crystalline lattice with long-range translational order but local rotational disorder (*30*). More precisely, the liquid-like behavior may generally represent the highly disordered and anharmonic motions of the strongly coupled vibrational modes of both PbX_3^- and A^+ sublattices (*31*). Here, we discuss three important consequences of the crystal-liquid duality: (i) The contrasting phonon and electron dynamics mean that lead halide perovskites belong to the family of solids called phonon glass electron crystals (PGECs) (*32*); (ii) the band-like charge transport, coupled with the liquid-like polarizability, means that a charge carrier can effectively form a large polaron (*33*), whose screened Coulomb potential reduces its scattering with charged defects and with other charge carriers; and (iii) large polaron formation, coupled with the phonon glass characteristics, may explain the much reduced cooling rates of hot carriers in HOIPs (*25*, *34*).

Department of Chemistry, Columbia University, New York, NY 10027, USA.
*Corresponding author. Email: xyzhu@columbia.edu

PHONON GLASS ELECTRON CRYSTAL

PGEC refers to a class of solids where charge transport is ballistic and phonon transport is diffusive. This ensures high electric conductivity but low thermal conductivity, the most desirable combination for efficient thermoelectrics. Since the initial proposal by Slack in 1995 (*35*), the PGEC concept has guided much research in thermoelectrics (*32*, *36*–*39*). A PGEC typically has large electronic bandwidth for efficient charge transport, whereas the phonon bands are disrupted by efficient scattering with local vibrations. At the limit of phonon disorder when the mean free path for phonon scattering is less than half of the phonon wavelength, we can essentially view nuclear motions in the solid as a collection of local vibrations (*32*, *39*), as is likely the case in HOIPs (*31*, *40*, *41*). Thermal transport occurs diffusively from the coupling of these local vibrations to their neighbors via damped oscillations.

The search for PGECs over the past 20 years has focused on semiconductors consisting of crystalline frameworks that determine their electronic band structures, but with pores enclosing weakly bound atoms or ions. A representative PGEC is the so-called type I clathrate compound, whose crystal structure consists of networked cages of tetrakaidecahedrons and dodecahedrons (Fig. 2A), each housing a group 1 or 2 guest atom "rattling" in the cage, as shown in Fig. 2 for $Ba_8Ga_{16}Ge_{30}$ (*32*). The motion of a rattling ion with respect to the cage with opposite charge can be represented by a varying dipole moment (Fig. 2B). The rattling in the nanocages introduces efficient scattering for the phonons, particularly acoustic phonons that are mainly responsible for thermal transport.

It is clear from the above definition that a lead halide perovskite crystal belongs to the PGEC material family. Here, the PbX_3^- sublattice

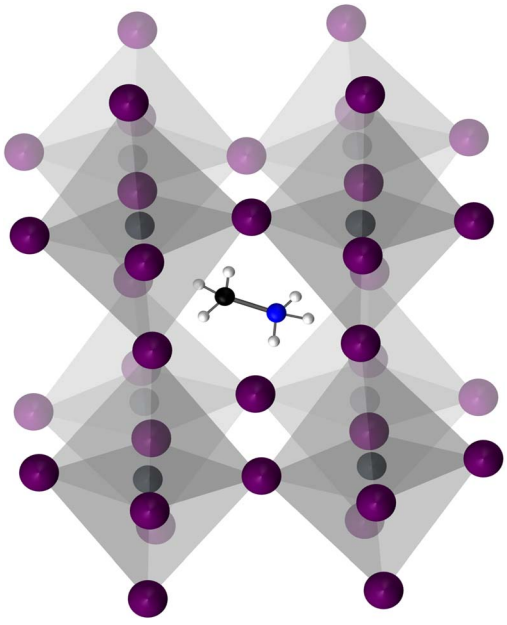

Fig. 1. Structure of $CH_3NH_3PbX_3$ perovskite. It consists of a framework of corner-sharing lead (gray) halide (purple) octahedrals and the $CH_3NH_3^+$ cation (black, blue, and white) in the nanocage.

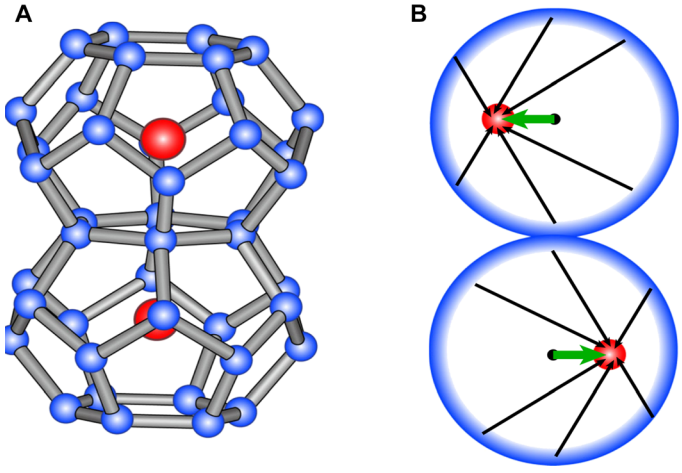

Fig. 2. Structure of a PGEC, $Ba_8Ga_{16}Ge_{30}$. (**A**) Two tetrakaidecahedron cages along the *z* direction consisting of anions and guest Ba^{2+} cation rattling against the anionic cage. (**B**) The cage (outer circles) and the symmetry-broken off-center guest atom compose an effective electric dipole moment (thick arrows), which is the vector sum of each dipole (thin arrows). Reprinted figure with permission from Takabatake *et al.* (*32*). Copyright 2014 by the American Physical Society.

forms the crystalline framework, whereas the A^+ cations "rattle" and/or "rotate" in the cuboctahedral cages (Fig. 1). The "phonon glass" character has come from various spectroscopic studies. Early NMR measurement on $CH_3NH_3PbX_3$ crystals revealed rapid rotational motion of $CH_3NH_3^+$ cations within the perovskite framework (*15*). The liquid-like behavior in the tetragonal and cubic phases is particularly apparent from the temperature-dependent dielectric function, which can be well described by the Kirkwood-Fröhlich equation originally developed for polar liquids (*16*). More recently, direct probe of phonon activities by neutron scattering (*17*, *19*, *20*), x-ray scattering (*18*, *21*, *26*), far-IR (*22*), terahertz (THz) (*23*), Raman (*17*, *23*, *24*), two-dimensional IR (*42*), and time-resolved optical Kerr effect (TR-OKE) (*25*, *43*) spectroscopies all revealed dynamic disorder, large anharmonicity, and overdamped vibrational motions. This dynamic behavior has been confirmed in molecular dynamics simulations (*31*, *44*–*46*). Here, we show two examples in time and frequency domains, respectively.

As the first example, Fig. 3 compares TR-OKE responses from three single-crystal lead halide perovskites—$MAPbBr_3$, $FAPbBr_3$, and their all-inorganic counterpart, $CsPbBr_3$—at room temperature. Note that at 295 K, both $MAPbBr_3$ and $FAPbBr_3$ are in the most disordered cubic phase, whereas $CsPbBr_3$ is in the most crystalline orthorhombic phase. In a TR-OKE experiment (*47*, *48*), shown schematically in the inset of Fig. 3A, a polarized laser pulse (pump) induces anisotropy in the refractive index and, thus, transient birefringence in the sample. After a controlled time delay, a probe laser pulse measures the decay in transient birefringence based on polarization rotation. This technique has been used in the past to probe liquids, particularly diffusive reorientation dynamics on picosecond time scales (*47*, *48*). In a crystalline solid, the TR-OKE transient is typically dominated by the ultrafast and nearly instantaneous electronic polarization, plus weaker coherent oscillations attributed to impulsively stimulated Raman excitation of phonons (*49*). The TR-OKE responses in Fig. 3 are more liquid-like than crystalline solid–like. Whereas the transient from $CsPbBr_3$ is dominated by the electronic response (laser cross-correlation) with a tail on the subpicosecond time scale, the transients from $MAPbBr_3$ and $FAPbBr_3$ feature broad and picosecond responses typical of diffusive motions in liquids. Note that, in the orthorhombic phase of $CsPbBr_3$, the crystalline behavior is revealed by the presence of coherent oscillation in the TR-OKE signal, which is particularly enhanced when the excitation photon energy moves closer to the bandgap (*43*).

The liquid-like behavior is also evident in the frequency domain, as shown by low-frequency Raman spectra of Yaffe *et al.* (*24*) for $CH_3NH_3PbBr_3$ and $CsPbBr_3$ crystals across the two phase transitions with increasing temperature (Fig. 4). Although the low-temperature orthorhombic phases (blue) of both crystals feature well-resolved phonon modes ($\leq$100 cm^{-1}), mainly of the lead bromide sublattice, the spectra become very diffuse and are dominated by a central peak in the tetragonal (green) and cubic (red) phases, indicating anharmonic and local polar fluctuations over broad time scales (*24*). Note that the phase transition temperatures of $CsPbBr_3$ are much higher than those of $CH_3NH_3PbBr_3$; at room temperature, the former is in the low-temperature orthorhombic phase, whereas the latter is in the high-temperature cubic phase.

The phonon glass characteristics, along with the respectable charge carrier mobilities reported to date, suggest that lead halide perovskites are promising candidates for thermoelectric materials (*31*, *40*, *41*, *50*–*52*). Experimental measurements (*53*–*56*) and dynamics simulations (*31*, *41*) revealed that thermal conductivities in HOIPs and their all-inorganic counterparts range from 10^{-1} to 10^{0} W m^{-1} K^{-1}, which are one to two orders of magnitude lower than those in conventional inorganic semiconductors but are rather similar to those of glasses or liquids (*57*). Kovalsky *et al.* (*54*) measured the thermal conductivity of $MAPbI_3$ that is a factor of 1.5 lower than that of $CsPbI_3$. The Debye model (that is, phonon gas model) effectively describes the thermal conductivity of both perovskites, consistent with the phonon glass characters, including the greater phonon disorder in $MAPbI_3$ than that in $CsPbI_3$. This phonon glass character and slow acoustic phonon transport may also contribute to the slow cooling of hot carriers, as discussed later.

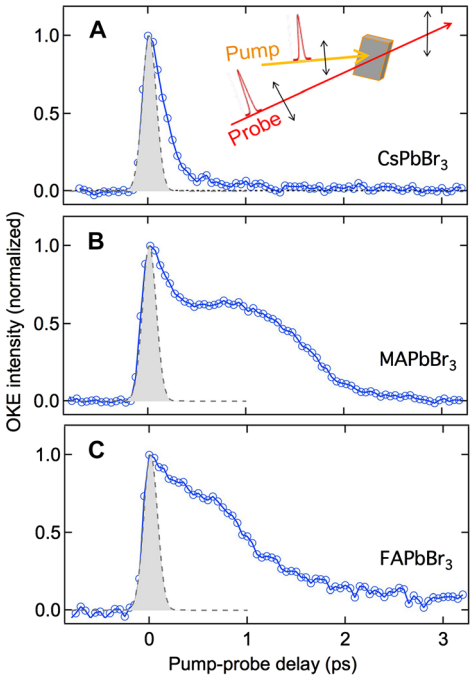

Fig. 3. TR-OKE probes liquid-like motions in lead halide perovskites. TR-OKE transients from single-crystal (**A**) $CsPbBr_3$, (**B**) $MAPbBr_3$, and (**C**) $FAPbBr_3$. The pump-probe cross-correlation is depicted as gray [full width at half-maximum (FWHM), 70 fs]. The inset in (A) illustrates the experimental setup. From Zhu *et al.* (*25*). Reprinted with permission from AAAS.

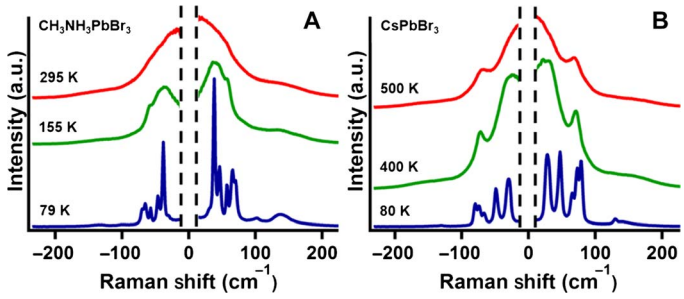

Fig. 4. Low-frequency Raman spectra of hybrid and inorganic lead halide perovskite crystals. $MAPbBr_3$ (**A**) and $CsPbBr_3$ (**B**) in the orthorhombic phase (blue), tetragonal phase (green), and cubic phase (red). Note that the phase transition temperatures for $CsPbBr_3$ are much higher than those for $MAPbBr_3$. The central peak characteristic of dynamic disordered, highly anharmonic, and dissipative vibrations grows with temperature in both materials. a.u., arbitrary units. Reprinted figure with permission from Yaffe *et al.* (*24*). Copyright 2017 by the American Physical Society.

DYNAMIC SCREENING AND LARGE POLARON FORMATION

The PGEC "crystal-liquid" duality shown in lead halide perovskites is likely critical to their success as optoelectronic materials through dynamic screening and large polaron formation. Because lead halide perovskite single crystals and thin films are typically grown from solutions at room temperature, a high density of defects is inevitable. However, these materials show exceptional defect tolerance, which leads to low charge carrier trapping and low nonradiative recombination rates (*58*) that are responsible for long carrier lifetimes and diffusion lengths. Zhu and Podzorov (*33*) posited that the key to understanding this lies in the realization that charge carriers in lead halide perovskites are not free carriers but are large polarons.

A polaron is an excess electron or hole dressed by polarization of nuclear coordinates in a crystalline lattice and is ubiquitous to polar and polarizable solids (*59*–*63*). For lead halide perovskites, we must consider charge formation and transport within the soft and ionic lattice with crystal-liquid duality. Given the exceptionally high polarizability of a soft lattice, a polaron must form for an excess charge. Two fundamental interaction potentials are responsible for polaron formation (*63*). The first is the long-range Coulomb potential (V^{LR}) between an excess charge and lattice ions, and the second is the short-range deformation potential (V^{SR}) that relates electronic energy to strain. If V^{SR} dominates, the result is a small polaron, with coherence length (L_{coh}) smaller than the unit cell dimension (a). When V^{LR} becomes more significant, L_{coh} is larger than a and the result is a large polaron. A large polaron is delocalized over multiple unit cells and its transport is coherent and band-like, with carrier mobility (μ) decreasing with increasing temperature (T), that is, $d\mu/dT < 0$. In contrast, a small polaron is localized to a unit cell and its transport occurs via thermally activated hopping, that is, $d\mu/dT > 0$.

The polarons in lead halide perovskites must be large polarons, because both transport and spectroscopic measurements showed $d\mu/dT < 0$ in broad temperature windows. Figure 5 shows the temperature-dependent charge carrier mobility obtained from Hall effect measurement on single-crystal $CH_3NH_3PbBr_3$ (*64*). In both tetragonal and cubic phases, the observed temperature dependences ($d\mu/dT < 0$) establish coherent transport, but the different scaling laws, $\mu \propto T^{-1.5}$ and $\mu \propto T^{-0.5}$, may suggest the dominance of different scattering mechanisms in the cubic and tetragonal phases, respectively (*64*). Similar scaling laws have been found from spectroscopic measurements on $CH_3NH_3PbI_3$ thin films (*65*–*68*).

A direct consequence of large polaron formation in lead halide perovskites is the efficient screening of the Coulomb potential. To understand the charge carrier properties, we consider the dielectric functions. Figure 6 shows the calculated dielectric functions for both $MAPbBr_3$ and $CsPbBr_3$ in the terahertz range (*43*). As the frequency decreases from >5 to ~1 THz, we see increases in the real part (ε_1) of the dielectric function by approximately one order of magnitude due to the activation of $PbBr_3^-$ longitudinal optical (LO) phonons. The positions of LO phonons are shown by the peaks in $\mathrm{Im}[-1/\varepsilon]$. The values of ε_1 are further increased in HOIPs by another factor of 2 as the frequency decreases to ~0.1 THz, due to the rotational motion of the dipolar methylammonium cations (*69*, *70*). The over one order of magnitude increase of ε_1 in lead halide perovskites is in stark contrast to what is known in conventional semiconductors, such as GaAs, where the corresponding increase in ε_1 is only ~20% (*57*). The large increase in ε_1 over the terahertz frequency range in HOIPs results in efficient screening of a nascent charge carrier on the subpicosecond time scale. Hence, for the resulting large polaron, all events requiring the Coulomb potential, such as scattering of a charge carrier with charged defects or other charge carriers, are inhibited. Electron-phonon coupling is also reflected in transport as localized shallow state (*71*–*74*), in spectroscopy by exciplex emission and polaron–to–free carrier transition in IR absorption (*75*), and macroscopically by photostriction (*76*). The coupling of methylammonium cation rotors to charge carriers is suggested by Gong *et al.* (*77*), who observed decreasing carrier lifetime with increasing moment of inertia when the methylammonium cation is deuterated.

Miyata *et al.* (*43*) provided a direct time-domain view of large polaron formation in single-crystal $MAPbBr_3$ and $CsPbBr_3$ using TR-OKE, with excitation photon energy above bandgap for charge injection (Fig. 7). On

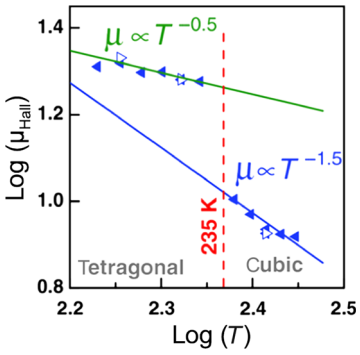

Fig. 5. Temperature dependence of Hall mobility in single-crystal $MAPbBr_3$. The fits to μ_{Hall} ($cm^2\ V^{-1}\ s^{-1}$) $\propto T\ (K)^{-\gamma}$ give $\gamma = 0.5$ in the tetragonal phase and $\gamma = 1.5$ in the cubic phase. From Yi *et al.* (*64*). Copyright Wiley-VCH Verlag GmbH & Co. KGaA. Reproduced with permission.

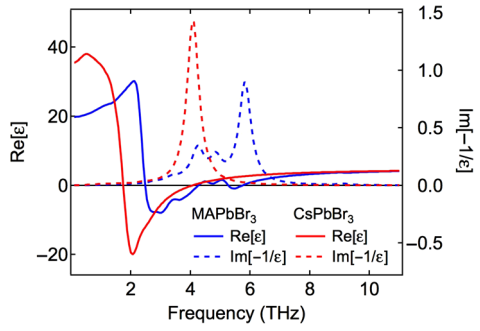

Fig. 6. Calculated dielectric functions of $MAPbBr_3$ (blue) and $CsPbBr_3$ (red). The solid and dashed curves show the real, Re[ε] (left), and imaginary, Im[−1/ε] (right), parts, respectively. From/adapted from Miyata *et al.* (*43*). Copyright The Authors, some rights reserved; exclusive licensee American Association for the Advancement of Science. Distributed under a Creative Commons Attribution NonCommercial License 4.0 (CC BY-NC) http://creativecommons.org/licenses/by-nc/4.0/.

the basis of the initial time constants for polaron formation, $\tau_{pol} = 0.3$ ps and 0.7 ps in $MAPbBr_3$ and $CsPbBr_3$, respectively, along with first-principles calculations, these authors concluded that large polarons form predominantly from the deformation of the $PbBr_3^-$ frameworks, irrespective of the cation type. Although there is more liquid-like disorder in the cubic $MAPbBr_3$ than in the orthorhombic $CsPbBr_3$, at room temperature, the intrinsic softness and polarizability of the PbX_3^- framework structure enables easy formation of large polarons upon charge injection in both HOIPs and their all-inorganic counterparts. HOIPs and their all-inorganic counterparts show similarly exceptional charge carrier properties for band edge carriers and solar cell performances (*78*–*83*).

LONG-LIVED HOT CARRIERS

One of the most striking observations in HOIPs is long-lived energetic carriers at low excitation densities (*25*, *34*). In a conventional polar semiconductor, excess electronic energy above the LO phonon energy is lost on ultrafast time scales of 100s fs due to the ubiquitous Coulomb potential, which governs the scattering of electrons with polar LO phonons (*84*, *85*). In GaAs, the electronic cooling rate $\langle dE/dt \rangle$ is of the order of 1 eV/ps for hot electrons with mean energy $\langle dE^* \rangle > E_{LO}$, where E_{LO} (=36 meV) is the LO phonon energy; this cooling process is slowed down by three to four orders of magnitude when $\langle dE^* \rangle$ falls below E_{LO} and scattering with acoustic phonons due to the deformation potential becomes dominant (*84*, *85*).

In contrast to GaAs, hot carriers with excess energy above the LO phonon energy are much longer-lived in HOIPs (*25*, *34*). Using time-resolved two-photon photoemission (TR-2PPE) spectroscopy and time-resolved photoluminescence (TR-PL), Zhu and co-workers found long-lived hot carriers in HOIPs at room temperature. The excess electronic energy of the order of 100 meV, which is much higher than E_{LO}, cools down at rates typical of acoustic phonon scattering, as shown in Fig. 8 for polycrystalline $MAPbI_3$ and single-crystal $MAPbBr_3$ (*25*, *34*). A comparison of HOIP single crystals with their all-inorganic counterpart at room temperature showed long-lived hot PL in $MAPbBr_3$ and $FAPbBr_3$, but not in $CsPbBr_3$ (*25*). This correlates well with the more liquid-like responses in $MAPbBr_3$ and $FAPbBr_3$ than in $CsPbBr_3$, as observed in TR-OKE measurements in Fig. 3. TR-2PPE measurement suggests a large polaron formation time of ~0.3 ps in $MAPbI_3$ (*34*), in agreement with the TR-OKE measurement for $MAPbBr_3$ (Fig. 7); this time scale is competitive with the initial LO phonon cooling time, leading to the partial retention of excess electronic energy. Although large polarons form in both $MAPbBr_3$ and $CsPbBr_3$ (*43*), the rate of formation is not competitive with phonon cooling in the latter. More recently, the presence of long-lived hot carriers has also been observed by Guo *et al.* (*86*) in $MAPbI_3$ thin films using transient absorption microscopy.

Monahan *et al.* (*87*) reported the observation of long-lived "warm" carriers (excess energy ~70 meV) on the 10-ps time scale in two-dimensional electronic spectroscopy of $MAPbI_3$. These authors showed strong coupling of charge carriers to a 0.9-THz phonon mode attributed to PbI_3^- lattice distortions (*87*), in excellent agreement with conclusions of Miyata *et al.* (*43*) on $MAPbBr_3$ and $CsPbBr_3$ from TR-OKE measurements. Monahan *et al.* (*87*) also observed long-lived coherence on the 10-ps time scale in the 0.9-THz phonon mode. It is possible that the large polaron formed from electron coupling to the PbI_3^- LO phonons further isolates the quasi-particle from the phonon glass environment, leading to long-lived coherence in the 0.9-THz mode. This interpretation finds support in a recent far-IR spectroscopy study of Ivanovska *et al.* (*88*), who observed very narrow absorption features in the terahertz region in photoexcited $MAPbI_3$. Further support for this idea can be found in the succinct analysis of Frost *et al.* (*89*), who argued that the transfer of phonon energy from the subset of optical phonons that are in quasi-equilibrium with the hot carrier to the acoustic phonon bath is inefficient due to the low thermal conductivity, a result of the phonon glass character. This analysis also explains the order-of-magnitude higher hot polaron cooling rate in $CsPbBr_3$ than in $MAPbBr_3$.

The slowed cooling of energetic carriers due to large polaron formation may be mechanistically different from the conventional phonon bottleneck effect. The latter occurs at high excitation densities when efficient scattering between hot carriers and LO phonons occurs, but the hot LO phonons are not cooled down by acoustic phonons at sufficiently high rate, that is, the bottleneck effect (*90*, *91*). As a result, the hot phonons can reheat the electrons/holes. The phonon bottleneck effect has been observed in $MAPbI_3$ thin films at high excitation densities ($\geq 10^{18}/cm^3$) (*92*–*94*). A marked difference between the conventional phonon bottleneck and the large polaron mechanism is seen in the excitation density dependences. In the conventional phonon bottleneck at $\rho_{ex} \geq 10^{18}/cm^3$ for $MAPbI_3$, the excess electronic energy at a given time increases with increasing ρ_{ex} (*92*–*94*). In contrast, the large polaron mechanism is most important at low excitation densities ($\rho_{ex} \leq 10^{18}/cm^3$) and the excess electronic energy decreases with increasing ρ_{ex} (Fig. 9)

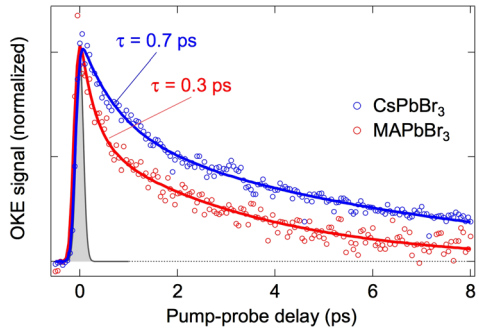

Fig. 7. Phonon dynamics triggered by photo-carrier injection as a function of pump-probe delay observed by TR-OKE with across-gap excitation. The TR-OKE responses for $MAPbBr_3$ (red circles) and $CsPbBr_3$ (blue circles) were obtained with excitation photon energies of 2.30 and 2.38 eV, respectively. The lines are double-exponential fits convoluted with a Gaussian function, which describes cross-correlation between the pump and the probe pulse (gray; FWHM, 70 fs). From/adapted from Miyata *et al.* (*43*). Copyright The Authors, some rights reserved; exclusive licensee American Association for the Advancement of Science. Distributed under a Creative Commons Attribution NonCommercial License 4.0 (CC BY-NC) http://creativecommons.org/licenses/by-nc/4.0/.

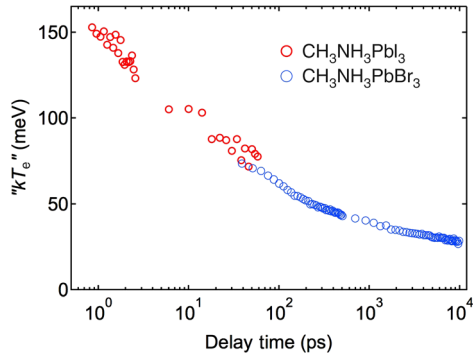

Fig. 8. Slow cooling of hot carriers in HOIPs. The data points are mean hot carrier energies from TR-2PPE of $MAPbI_3$ thin films (red) (*34*) and TR-PL of $MAPbBr_3$ single crystals (blue) (*25*). In the latter, a background offset due to intrinsic broadening in PL spectra has been subtracted. The excess excitation energy (above bandgap) is 1.0 eV for $MAPbI_3$ and 0.8 eV for $MAPbBr_3$.

(*34*). With increasing excitation density, the mutual repulsive interaction destabilizes the large polarons (*63*); this is essentially a depolarization effect, leading to the reduction in the magnitude of the Coulomb screening and/or enhancement of the coupling of hot polarons to the phonon glass environment. As pointed out by Frost *et al.* (*89*), the transition density of $\rho_{ex} \sim 10^{18}/cm^3$ is essentially the critical Mott density when the large polarons start to overlap spatially.

The long-lived hot carriers in HOIPs may provide two potential advantages in solar cells. The first is the realization of the so-called hot carrier solar cell, with a theoretical power conversion efficiency (η) as high as 66% (*95*–*97*). For comparison, a conventional solar cell harvests carriers only at the band edges and the loss of excess electronic energy (from the absorption of above-bandgap photons) is partially responsible for the Shockley-Queisser limit of η ~ 33% (*98*). On the basis of the partial retention of hot carrier energy, Niesner *et al.* (*34*) estimated an upper limit of η ~ 38% from $MAPbI_3$ when hot carriers are harvested. The second advantage results from the excess kinetic energy. A portion of carriers generated from the absorption of sunlight are hot polarons. The higher kinetic energy of hot polarons may allow for easier transport across energetic barriers at domain boundaries or interfaces, leading to a higher photocurrent seen in HOIP solar cells.

DEFECT TOLERANCE

Efficient screening and large polaron formation in lead halide perovskites are key to the most significant advantage of lead halide perovskite as a semiconductor, that is, defect tolerance (*99*–*102*). The defect tolerance leads to long carrier lifetimes and diffusion lengths responsible for their exceptional performance in solar cells and light-emitting devices (*1*–*5*, *103*–*106*). Quantitative measurements of PL intensity (*79*) or photoconductivity (*58*) as a function of excitation density revealed low first-order nonradiative recombination rates. The latter is illustrated by the scaling of photoconductivity (σ) with excitation density (*G*, proportional to incident photon flux, *F*), $\sigma \propto G^{\alpha}$ or F^{α}, in the four-probe measurement of Chen *et al.* (*58*) in either vapor-grown polycrystalline $MAPbI_3$ thin film or single-crystal $MAPbBr_3$ (Fig. 10). For excitation density varying over three orders of magnitude, the data can be well described by $\alpha = {}^1/_2$ expected for radiative recombination, as opposed to $\alpha = 1$ for trap-mediated nonradiative recombination. The low nonradiative recombination rate exists in both HOIPs and their all-inorganic counterparts; for band edge carriers, the different large polaron formation rates on the picosecond time scales are not expected to affect the properties of band edge carriers with nanosecond to microsecond lifetimes (*79*).

We can understand the defect tolerance from two perspectives. From a carrier perspective, a free band carrier is rapidly protected on the pico- or subpicosecond time scale to form a large polaron (*43*), whose screened Coulomb potential drastically reduces its scattering with a charged defect or a trapped charge of opposite sign on an originally neutral defect. The latter scenario means that the well-known Shockley-Read-Hall (SRH) mechanism (*107*, *108*) for nonradiative recombination is diminished. From a defect perspective, the high polarizability in the soft and ionic lattice, including ion mobility on long time scales, can lead to the sufficient screening and compensation of charged defects in a lead halide perovskite lattice (*69*, *109*–*111*). As a result, the traps are energetically shallow and electrostatically screened (*100*, *102*), thus diminishing the role of these traps in SRH recombination.

The conventional wisdom to reduce defects in semiconductor technology is to achieve perfection, as exemplified by single-crystal silicon with remarkably low defect densities. However, this requirement cannot be met by emerging semiconductors made from molecular, hybrid, or nanocrystalline materials, where room temperature and solution synthesis/processing conditions inevitably result in a high density of defects that are detrimental to their performance. The exceptional defect tolerance in lead halide perovskites suggests that dynamic screening in intrinsically "soft" and polarizable materials provides a design principle to achieve defect tolerance, thus turning imperfection to perfection.

LARGE POLARON TRANSPORT

The "electron crystal" nature of lead halide perovskites is established by the band-like transport of charge carriers, particularly with charge mobility (μ) scaling with temperature (*T*) by $\mu \propto T^{-1.5}$, as determined directly by Hall effect measurements for $MAPbBr_3$ in the cubic phase (*64*), as well as by microwave, gigahertz, and terahertz spectroscopies on polycrystalline $MAPbI_3$ (*65*–*68*). The decreasing mobility with temperature ($d\mu/dT < 0$) unambiguously establishes coherent transport, as expected from large polarons, in stark contrast to thermally activated transport of small polarons (*63*).

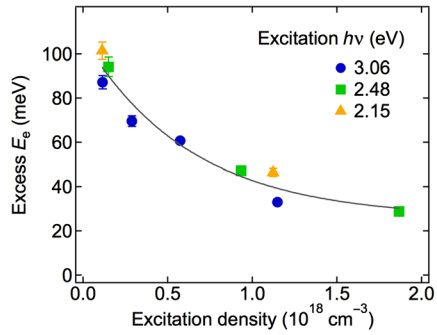

Fig. 9. Excitation density dependence of excess electronic energy in $MAPbI_3$. The data points are from TR-PL in the initial 0- to 20-ps time window (time resolution) of a vapor-deposited $MAPbI_3$ thin film. PL at three excitation photon energies, $h\nu$ = 3.06 eV (blue), 2.48 eV (green), and 2.15 eV (orange). The gray curve is an exponential fit to the data points. The *y* axis is excess electronic energy, referenced to the asymptotic value at long times (~0.5 ns). Reprinted (adapted) with permission from Niesner *et al.* (*34*). Copyright (2016) American Chemical Society.

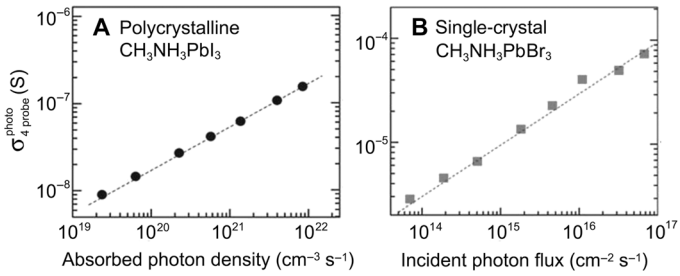

Fig. 10. Excitation density–dependent photoconductivity shows little charge carrier trapping. (**A**) Photoconductivity measured in a vapor-grown 100-nm-thick polycrystalline $CH_3NH_3PbI_3$ film as a function of absorbed photon density. (**B**) Photoconductivity measured as a function of incident photon flux in a macroscopic single-crystal $CH_3NH_3PbBr_3$ with a (dark) Hall mobility $\mu_{Hall} \approx 60$ cm^2 V^{-1} s^{-1} (for holes). Dashed lines are the power law fits with exponent $\alpha = {}^1/_2$: $\sigma \propto G^\alpha$ or F^α. Reprinted with permission from Chen *et al.* (*58*). Copyright (2016) Nature Commun.

For lead halide perovskites, the valence and conduction bands are determined mainly by the PbX_3^- sublattice, with the A^+ cation sublattice modulating the band structure electrostatically and through electron-phonon coupling. Electronic structure calculations predict large valence and conduction band dispersions that yield low electron/hole masses of 0.1 to 0.15 m_e (*112*–*114*). This low band mass is confirmed by magneto optical absorption measurement, which gives the reduced e-h (exciton) mass from the Landau levels (*115*). Whereas the experimentally determined $\mu \propto T^{-1.5}$ scaling law agrees with prediction from acoustic phonon scattering in nonpolar semiconductors (*116*), analysis based on acoustic phonon scattering yields charge carrier mobilities (μ) of the order of 10^3 cm^2 V^{-1} s^{-1} (*51*, *117*–*119*), only slightly lower than those predicted from band masses and still more than one order of magnitude higher than experimental values.

It has been suggested that scattering with optical phonons is more important than that with acoustic phonons in limiting mobility in HOIPs (*120*, *121*). The scattering of charge carriers with optical phonons has been traditionally treated within the polaron theory of Fröhlich (*61*), which was subsequently extended by Feynman (*62*). Here, a unit-less parameter ($\alpha_{e\text{-}ph}$) is introduced to describe the strength of electron LO phonon coupling

$$\alpha_{e-ph} = \frac{1}{2}\left(\frac{1}{\varepsilon_\infty} - \frac{1}{\varepsilon_0}\right)\frac{k_e e^2}{\hbar\omega_{LO}}\left(\frac{2m^*\omega_{LO}}{\hbar}\right)^{1/2} \quad (1)$$

where ε_∞ and ε_0 are the optical and static dielectric constants, respectively; k_e is the Coulomb's law constant; $\hbar$ is the Planck's constant; ω_{LO} is the LO phonon frequency; and m^* is the band mass of electron or hole. To the first-order approximation, the renormalized carrier mass, that is, polaron mass (m_p), is given by

$$m_p \backsimeq m^*(1 + \alpha_{e-ph}/6) \quad (2)$$

On the basis of the mean LO phonon frequencies and the dielectric constants for HOIPs, several groups (*22*, *45*, *58*) estimated the electron-phonon coupling constants of $\alpha_{e\text{-}ph}$ = 1.7 to 2.4, which corresponds to intermediate coupling.

From Eq. 2, we obtain m_p in the range of 1.3 to 1.4 m^*. The corresponding polaron radii, $R_p = h^{1/2}/(2cm^*\omega_{LO})^{1/2}$, are in the range of 3 to 5 nm for HOIPs (*22*); thus, the diameter of the large polaron is ~10× the unit cell dimension. We estimate the polaron binding energy from the polaron radius to be of the order of 10 to 100 meV, depending on the dielectric constant used (see Fig. 6). The large polarons discussed here are in contrast to the tightly bound small polarons from the computational study of Neukirch *et al.* (*122*). These small polarons are likely minority trapped charges, not the charge carriers responsible for transport.

The LO phonons are highly populated in HOIPs at room temperature because of their low frequencies (*22*, *43*). Under this condition, it is appropriate to use the general equations of Feynman-Ōsaka (*62*, *123*) to calculate electron and hole polaron mobilities. Miyata *et al.* (*43*) obtained μ_e = 149.8 cm^2 V^{-1} s^{-1} and μ_h = 79.2 cm^2 V^{-1} s^{-1} in $CH_3NH_3PbBr_3$; the corresponding values in $CsPbBr_3$ are μ_e = 48.2 cm^2 V^{-1} s^{-1} and μ_h = 41.3 cm^2 V^{-1} s^{-1}. Similarly, Sendner *et al.* (*22*) calculated average electron-hole mobilities of μ = 50, 150, and 200 ± 30 cm^2 V^{-1} s^{-1} for $MAPbCl_3$, $MAPbBr_3$, and $MAPbI_3$, respectively, and Frost (*124*) calculated electron and hole polaron mobilities in $MAPbI_3$ of 136 and 94 cm^2 V^{-1} s^{-1}, respectively. The calculated mobility values for HOIPs are slightly higher than those reported from experimental studies. For single-crystal $MAPbBr_3$ and $MAPbI_3$ at room temperature, the reported μ values are 10 to 115 cm^2 V^{-1} s^{-1} and 24 to 164 cm^2 V^{-1} s^{-1}, respectively (*8*, *9*, *58*, *64*, *125*). Whereas a large polaron is formed mainly from the deformation of the PbX_3^- sublattice, a moving large polaron is further slowed down from dielectric loss to the disordered vibrations at lower frequencies attributed to cation motions. In HOIPs, this additional dielectric loss channel occurs at ~0.1 THz, where the rotational motions of the dipolar MA^+ cations are activated, leading to another step increase by ~2× in ε_1 (*70*). This loss process is called "dielectric drag" for ion movement in polar liquids (*126*). In related work, Anusca *et al.* (*70*) suggested that the two-tiered dielectric responses led to a "hyperpolaron" as a result of the additional screening of a Fröhlich polaron by the liquid-like MA^+ cation motions.

RADIATIVE RECOMBINATION

The bimolecular radiative recombination rate constants are of the order $k_2 = 10^{-10}$ cm^3 s^{-1} in both HOIPs and their all-inorganic counterparts (*58*, *79*, *127*). There have been arguments that these rate constants are

about five orders of magnitude lower than that predicted from the Langevin model. The Langevin model (*128*) is typically used to describe bimolecular recombination in low-mobility and disordered systems (*129*), where the recombination rate can be calculated from the Coulomb capture radius (r_c), that is, the e-h distance for which the Coulomb potential is equal to the thermal energy. However, the Langevin model does not actually apply to lead halide perovskites because of the band-like transport with modest (~10 to 100 $cm^2\ V^{-1}\ s^{-1}$), not low (<1 $cm^2\ V^{-1}\ s^{-1}$), mobilities.

The perceived low values in radiative recombination rate constants that are partially responsible for long carrier lifetime and diffusion length have also led to discussions on the indirect character of bandgap in HOIPs. A particular argument attributes the indirect bandgap character to large Rashba splitting (*130*–*133*). Because of strong spin-orbital coupling in the presence of heavy atoms, the conduction band and the valence band may be spin-polarized. In the presence of local electric field resulting from electrostatic ordering (*110*, *134*) and static or dynamic symmetry breaking (*130*–*132*), electrons with different spins ($m_s = \pm^1/_2$) experience opposite forces from electromagnetic interaction. This leads to the splitting of conduction band and (to a lesser extent) the valence band in momentum space, thus introducing indirect bandgap character. Experimentally, the indirect bandgap is believed to lie at 47 to 75 meV below the direct bandgap in $MAPbI_3$, as obtained from temperature-dependent PL (*65*, *135*) and pressure-dependent absorption and PL (*136*). Numerical simulations also addressed the disparate roles of direct and indirect bandgaps in absorption and emission (*137*).

Here, we present an alternative mechanism to explain the indirect bandgap character. As argued by Chen *et al.* (*58*), a model more appropriate than the Langevin model to describe radiative recombination in lead halide perovskites is the van Roosbroeck–Shockley theory (*138*), which obtains the radiative recombination rate from detailed balance under thermal equilibrium in the dark (*138*, *139*). The van Roosbroeck–Shockley theory gives k_2 only approximately one order of magnitude higher than experimental values; this difference can be well accounted for by polaron formation (*58*). The equilibrium carrier concentration is increased upon polaron formation by the stabilization of a charge carrier and the increased density of states resulting from deviation from parabolic dispersion. These effects decrease k_2 from the van Roosbroeck–Shockley theory by approximately one order of magnitude, leading to good agreement with experimental values (*58*). For a polaron stabilization energy within 2 to 3 kT at room temperature, there is a dynamic equilibrium between large polarons and free carriers. The electron and hole large polarons are expected to be located in spatially separate regions, due to their opposite effects on the bending of Pb-X-Pb (*43*), as well as their opposite effects in dipolar polarization (*58*, *110*, *134*); in this sense, the indirect character of the bandgap is in real space, not in the momentum space. As a result, the radiative recombination rate from the energetically stabilized large polarons is expected to be much lower than that from free band carriers. This can give rise to thermally activated PL (*65*, *135*). The lower transition strength for the radiative recombination from the e-h polaron states can also appear in absorption due to electron-phonon coupling in the absorption process (*136*, *140*). Besides the large polaron–free carrier equilibrium, there is an equilibrium between carriers and excitons with binding energies of the order of kT at room temperature (*5*, *10*, *69*, *141*, *142*) and the carriers and excitons may be located in spatially separate regions in a heterogeneous environment of a polycrystalline thin film (*143*). All these effects may contribute to the apparent thermal activation in PL measurements.

SUMMARY AND OUTLOOK

In this perspective, we attempt a unified view of the optoelectronic properties of lead halide perovskites from their unique crystal-liquid duality. We show that lead halide perovskites belong to the PGEC family due to the binary structure consisting of a cage-like PbX_3^- sublattice and a more weakly bound A^+ cation sublattice. This PGEC character gives rise to the remarkable contrast in the transport properties of carrier and phonons. In particular, the thermal transport in lead halide perovskites, particularly HOIPs, is diffusive because of the liquid-like dynamic disorder in the phonon manifold, whereas charge transport is ballistic and band-like in the PbX_3^- sublattice. The partial localization of a band carrier in the PbX_3^- phonon environment leads to the formation of a large polaron, whose screened Coulomb potential reduces its scattering with charged defects and other charge carriers. The effective Coulomb screening can be found in the dielectric function, which, in HOIPs, increases by more than an order of magnitude as frequency decreases from optical to the terahertz region. We can account for the modest mobility of the large polarons by the low frequencies of PbX_3^- LO phonons that are highly populated at room temperature and to additional dielectric loss to the disordered vibrations of the cation sublattice. Large polaron formation and the phonon glass character may also explain the long lifetimes of hot carriers in HOIPs. The understanding presented here suggests a new design principle for high performance and defect-tolerant semiconductors from PGEC type of structures with liquid-like dielectric functions.

REFERENCES AND NOTES

1. W. Zhang, G. E. Eperon, H. J. Snaith, Metal halide perovskites for energy applications. *Nat. Energy* **1**, 16048 (2016).
2. N.-G. Park, T. Miyasaka, M. Grätzel, *Organic-Inorganic Halide Perovskite Photovoltaics* (Springer, 2016).
3. S. A. Veldhuis, P. P. Boix, N. Yantara, M. Li, T. C. Sum, N. Mathews, S. G. Mhaisalkar, Perovskite materials for light-emitting diodes and lasers. *Adv. Mater.* **28**, 6804–6834 (2016).
4. B. R. Sutherland, E. H. Sargent, Perovskite photonic sources. *Nat. Photonics* **10**, 295–302 (2016).
5. J. S. Manser, J. A. Christians, P. V. Kamat, Intriguing optoelectronic properties of metal halide perovskites. *Chem. Rev.* **116**, 12956–13008 (2016).
6. T. M. Brenner, D. A. Egger, L. Kronik, G. Hodes, D. Cahen, Hybrid organic–inorganic perovskites: Low-cost semiconductors with intriguing charge-transport properties. *Nat. Rev. Mater.* **1**, 15007 (2016).
7. G. Xing, N. Mathews, S. Sun, S. S. Lim, Y. M. Lam, M. Grätzel, S. Mhaisalkar, T. C. Sum, Long-range balanced electron- and hole-transport lengths in organic-inorganic $CH_3NH_3PbI_3$. *Science* **342**, 344–347 (2013).
8. Q. Dong, Y. Fang, Y. Shao, P. Mulligan, J. Qiu, L. Cao, J. Huang, Electron-hole diffusion lengths > 175 um in solution-grown $CH_3NH_3PbI_3$ single crystals. *Science* **347**, 967–970 (2015).
9. D. Shi, V. Adinolfi, R. Comin, M. Yuan, E. Alarousu, A. Buin, Y. Chen, S. Hoogland, A. Rothenberger, K. Katsiev, Y. Losovyj, X. Zhang, P. A. Dowben, O. F. Mohammed, E. H. Sargent, O. M. Bakr, Low trap-state density and long carrier diffusion in organolead trihalide perovskite single crystals. *Science* **347**, 519–522 (2015).
10. L. M. Herz, Charge-carrier dynamics in organic-inorganic metal halide perovskites. *Annu. Rev. Phys. Chem.* **67**, 65–89 (2016).
11. T. Leijtens, G. E. Eperon, A. J. Barker, G. Grancini, W. Zhang, J. M. Ball, A. R. S. Kandada, H. J. Snaith, A. Petrozza, Carrier trapping and recombination: The role of defect physics in enhancing the open circuit voltage of metal halide perovskite solar cells. *Energy Environ. Sci.* **9**, 3472–3481 (2016).
12. D. B. Mitzi, Solution-processed inorganic semiconductors. *J. Mater. Chem.* **14**, 2355–2365 (2004).
13. Y. Rakita, S. R. Cohen, N. K. Kedem, G. Hodes, D. Cahen, Mechanical properties of $APbX_3$ (*A*=Cs or CH_3NH_3; *X*=I or Br) perovskite single crystals. *MRS Commun.* **5**, 623–629 (2015).
14. T. Baikie, Y. Fang, J. M. Kadro, M. Schreyer, F. Wei, S. G. Mhaisalkar, M. Graetzeld, T. J. White, Synthesis and crystal chemistry of the hybrid perovskite $(CH_3NH_3)\ PbI_3$ for solid-state sensitised solar cell applications. *J. Mater. Chem. A* **1**, 5628–5641 (2013).

15. R. E. Wasylishen, O. Knop, J. B. Macdonald, Cation rotation in methylammonium lead halides. *Solid State Commun.* **56**, 581–582 (1985).
16. N. Onoda-Yamamuro, T. Matsuo, H. Suga, Dielectric study of $CH_3NH_3PbX_3$ (X = Cl, Br, I). *J. Phys. Chem. Solids* **53**, 935–939 (1992).
17. A. Létoublon, S. Paofai, B. Rufflé, P. Bourges, B. Hehlen, T. Michel, C. Ecolivet, O. Durand, S. Cordier, C. Katan, J. Even, Elastic constants, optical phonons, and molecular relaxations in the high temperature plastic phase of the $CH_3NH_3PbBr_3$ hybrid perovskite. *J. Phys. Chem. Lett.* **7**, 3776–3784 (2016).
18. H. Mashiyama, Y. Kurihara, T. Azetsu, Disordered cubic perovskite structure of $CH_3NH_3PbX_3$ (X= Cl, Br, I). *J. Korean Phys. Soc.* **32**, S156–S158 (1998).
19. T. Chen, B. J. Foley, B. Ipek, M. Tyagi, J. R. D. Copley, C. M. Brown, J. J. Choib, S.-H. Lee, Rotational dynamics of organic cations in the $CH_3NH_3PbI_3$ perovskite. *Phys. Chem. Chem. Phys.* **17**, 31278–31286 (2015).
20. I. P. Swainson, C. Stock, S. F. Parker, L. Van Eijck, M. Russina, J. W. Taylor, From soft harmonic phonons to fast relaxational dynamics in $CH_3NH_3PbBr_3$. *Phys. Rev. B* **92**, 100303 (2015).
21. A. N. Beecher, O. E. Semonin, J. M. Skelton, J. M. Frost, M. W. Terban, H. Zhai, A. Alatas, J. S. Owen, A. Walsh, S. J. L. Billinge, Direct observation of dynamic symmetry breaking above room temperature in methylammonium lead iodide perovskite. *ACS Energy Lett.* **1**, 880–887 (2016).
22. M. Sendner, P. K. Nayak, D. A. Egger, S. Beck, C. Müller, B. Epding, W. Kowalsky, L. Kronik, H. J. Snaith, A. Pucci, R. Lovrinčić, Optical phonons in methylammonium lead halide perovskites and implications for charge transport. *Mater. Horizons* **3**, 613–620 (2016).
23. A. M. A. Leguy, A. R. Goñi, J. M. Frost, J. Skelton, F. Brivio, X. Rodríguez-Martínez, O. J. Weber, A. Pallipurath, M. I. Alonso, M. Campoy-Quiles, M. T. Weller, J. Nelson, A. Walsh, P. R. F. Barnes, Dynamic disorder, phonon lifetimes, and the assignment of modes to the vibrational spectra of methylammonium lead halide perovskites. *Phys. Chem. Chem. Phys.* **18**, 27051–27066 (2016).
24. O. Yaffe, Y. Guo, L. Z. Tan, D. A. Egger, T. Hull, C. C. Stoumpos, F. Zheng, T. F. Heinz, L. Kronik, M. G. Kanatzidis, J. S. Owen, A. M. Rappe, M. A. Pimenta, L. E. Brus, Local polar fluctuations in lead halide perovskite crystals. *Phys. Rev. Lett.* **118**, 136001 (2017).
25. H. Zhu, K. Miyata, Y. Fu, J. Wang, P. P. Joshi, D. Niesner, K. W. Williams, S. Jin, X. Y. Zhu, Screening in crystalline liquids protects energetic carriers in hybrid perovskites. *Science* **353**, 1409–1413 (2016).
26. M. T. Weller, O. J. Weber, P. F. Henry, A. M. Di Pumpo, T. C. Hansen, Complete structure and cation orientation in the perovskite photovoltaic methylammonium lead iodide between 100 and 352 K. *Chem. Commun.* **51**, 4180–4183 (2015).
27. A. Poglitsch, D. Weber, Dynamic disorder in methylammoniumtrihalogenoplumbates (II) observed by millimeter-wave spectroscopy. *J. Chem. Phys.* **87**, 6373 (1987).
28. S. Hirotsu, J. Harada, M. Iizumi, K. Gesi, Structural phase transitions in $CsPbBr_3$. *J. Phys. Soc. Jpn.* **37**, 1393–1398 (1974).
29. J. Even, M. Carignano, C. Katan, Molecular disorder and translation/rotation coupling in the plastic crystal phase of hybrid perovskites. *Nanoscale* **8**, 6222–6236 (2016).
30. J. Timmermans, Un nouvel état mésomorphe les cristaux organiques plastiques. *J. Chim. Phys.* **35**, 331–344 (1938).
31. L. D. Whalley, J. M. Skelton, J. M. Frost, A. Walsh, Phonon anharmonicity, lifetimes, and thermal transport in $CH_3NH_3PbI_3$ from many-body perturbation theory. *Phys. Rev. B* **94**, 220301(R) (2016).
32. T. Takabatake, K. Suekuni, T. Nakayama, E. Kaneshita, Phonon-glass electron-crystal thermoelectric clathrates: Experiments and theory. *Rev. Mod. Phys.* **86**, 669–716 (2014).
33. X.-Y. Zhu, V. Podzorov, Charge carriers in hybrid organic–inorganic lead halide perovskites might be protected as large polarons. *J. Phys. Chem. Lett.* **6**, 4758–4761 (2015).
34. D. Niesner, H. Zhu, K. Miyata, P. P. Joshi, T. J. S. Evans, B. J. Kudisch, M. T. Trinh, M. Marks, X.-Y. Zhu, Persistent energetic electrons in methylammonium lead iodide perovskite thin films. *J. Am. Chem. Soc.* **138**, 15717–15726 (2016).
35. G. A. Slack, *CRC Handbook of Thermoelectrics* (CRC Press, 1995).
36. H. Liu, X. Shi, F. Xu, L. Zhang, W. Zhang, L. Chen, Q. Li, C. Uher, T. Day, G. J. Snyder, Copper ion liquid-like thermoelectrics. *Nat. Mater.* **11**, 422–425 (2012).
37. B. C. Sales, D. Mandrus, R. K. Williams, Filled skutterudite antimonides: A new class of thermoelectric materials. *Science* **272**, 1325–1328 (1996).
38. X. Shi, J. Yang, J. R. Salvador, M. Chi, J. Y. Cho, H. Wang, S. Bai, J. Yang, W. Zhang, L. Chen, Multiple-filled skutterudites: High thermoelectric figure of merit through separately optimizing electrical and thermal transports. *J. Am. Chem. Soc.* **133**, 7837–7846 (2011).
39. M. Beekman, D. T. Morelli, G. S. Nolas, Better thermoelectrics through glass-like crystals. *Nat. Mater.* **14**, 1182–1185 (2015).
40. T. Hata, G. Giorgi, K. Yamashita, The effects of the organic–inorganic interactions on the thermal transport properties of $CH_3NH_3PbI_3$. *Nano Lett.* **16**, 2749–2753 (2016).
41. M. Wang, S. Lin, Anisotropic and ultralow phonon thermal transport in organic–inorganic hybrid perovskites: Atomistic insights into solar cell thermal management and thermoelectric energy conversion efficiency. *Adv. Funct. Mater.* **26**, 5297–5306 (2016).
42. A. A. Bakulin, O. Selig, H. J. Bakker, Y. L. A. Rezus, C. Müller, T. Glaser, R. Lovrincic, Z. Sun, Z. Chen, A. Walsh, J. M. Frost, T. L. C. Jansen, Real-time observation of organic cation reorientation in methylammonium lead iodide perovskites. *J. Phys. Chem. Lett.* **6**, 3663–3669 (2015).
43. K. Miyata, D. Meggiolaro, M. T. Trinh, P. P. Joshi, E. Mosconi, S. C. Jones, F. De Angelis, X.-Y. Zhu, Large polarons in lead halide perovskites. *Sci. Adv.* **3**, e1701217 (2017).
44. E. Mosconi, J. M. Azpiroz, F. De Angelis, Ab initio molecular dynamics simulations of methylammonium lead iodide perovskite degradation by water. *Chem. Mater.* **27**, 4885–4892 (2015).
45. J. M. Frost, A. Walsh, What is moving in hybrid halide perovskite solar cells? *Acc. Chem. Res.* **49**, 528–535 (2016).
46. A. Mattoni, A. Filippetti, C. Caddeo, Modeling hybrid perovskites by molecular dynamics. *J. Phys. Condens. Matter* **29**, 043001 (2016).
47. D. McMorrow, W. T. Lotshaw, G. A. Kenney-Wallace, Femtosecond optical Kerr studies on the origin of the nonlinear responses in simple liquids. *IEEE J. Quant. Electron.* **24**, 443–454 (1988).
48. R. Righini, Ultrafast optical Kerr effect in liquids and solids. *Science* **262**, 1386–1390 (1993).
49. K. Polok, B. Ratajska-Gadomska, J. Konarska, W. Gadomski, Coherent optical phonons in pure and Pr^{3+} doped YAG crystal studied by optical Kerr effect spectroscopy: Temperature and concentration dependence. *Chem. Phys.* **442**, 119–127 (2014).
50. A. Filippetti, C. Caddeo, P. Delugas, A. Mattoni, Appealing Perspectives of hybrid lead–iodide perovskites as thermoelectric materials. *J. Phys. Chem. C* **120**, 28472–28479 (2016).
51. Y. He, G. Galli, Perovskites for solar thermoelectric applications: A first principle study of $CH_3NH_3Al_3$ (A = Pb and Sn). *Chem. Mater.* **26**, 5394–5400 (2014).
52. X. Mettan, R. Pisoni, P. Matus, A. Pisoni, J. Jaćimović, B. Náfrádi, M. Spina, D. Pavuna, L. Forró, E. Horváth, Tuning of the thermoelectric figure of merit of $CH_3NH_3MI_3$ (M=Pb, Sn) photovoltaic perovskites. *J. Phys. Chem. C* **119**, 11506–11510 (2015).
53. A. Pisoni, J. Jaćimović, O. S. Barišić, M. Spina, R. Gaál, L. Forró, E. Horváth, Ultra-low thermal conductivity in organic–inorganic hybrid perovskite $CH_3NH_3PbI_3$. *J. Phys. Chem. Lett.* **5**, 2488–2492 (2014).
54. A. Kovalsky, L. Wang, G. T. Marek, C. Burda, J. S. Dyck, Thermal conductivity of $CH_3NH_3PbI_3$ and $CsPbI_3$: Measuring the effect of the methylammonium ion on phonon scattering. *J. Phys. Chem. C* **121**, 3228–3233 (2017).
55. Z. Guo, S. J. Yoon, J. S. Manser, P. V. Kamat, T. Luo, Structural phase-and degradation-dependent thermal conductivity of $CH_3NH_3PbI_3$ perovskite thin films. *J. Phys. Chem. C* **120**, 6394–6401 (2016).
56. W. Lee, H. Li, A. B. Wong, D. Zhang, M. Lai, Y. Yu, Q. Kong, E. Lin, J. J. Urban, J. C. Grossman, P. Yang, Ultralow thermal conductivity in all-inorganic halide perovskites. *Proc. Natl. Acad. Sci. U.S.A.* **114**, 8693–8697 (2017).
57. M. S. Shur, *Handbook Series on Semiconductor Parameters* (World Scientific, 1996), vol. 1.
58. Y. Chen, H. T. Yi, X. Wu, R. Haroldson, Y. N. Gartstein, Y. I. Rodionov, K. S. Tikhonov, A. Zakhidov, X.-Y. Zhu, V. Podzorov, Extended carrier lifetimes and diffusion in hybrid perovskites revealed by Hall effect and photoconductivity measurements. *Nat. Commun.* **7**, 12253 (2016).
59. L. Landau, On the motion of electrons in a crystal lattice. *Phys. Z. Sowjetunion* **3**, 664 (1933).
60. T. Holstein, Studies of polaron motion: Part I. The molecular-crystal model. *Ann. Phys.* **8**, 325–342 (1959).
61. H. Fröhlich, Electrons in lattice fields. *Adv. Physiol. Educ.* **3**, 325–361 (1954).
62. R. P. Feynman, Slow electrons in a polar crystal. *Phys. Rev.* **97**, 660 (1955).
63. D. Emin, *Polarons* (Cambridge Univ. Press, 2013).
64. H. T. Yi, X. Wu, X.-Y. Zhu, V. Podzorov, Intrinsic charge transport across phase transitions in hybrid organo-inorganic perovskites. *Adv. Mater.* **28**, 6509–6514 (2016).
65. T. J. Savenije, C. S. Ponseca Jr., L. Kunneman, M. Abdellah, K. Zheng, Y. Tian, Q. Zhu, S. E. Canton, I. G. Scheblykin, T. Pullerits, A. Yartsev, V. Sundström, Thermally activated exciton dissociation and recombination control the carrier dynamics in organometal halide perovskite. *J. Phys. Chem. Lett.* **5**, 2189–2194 (2014).
66. M. Karakus, S. A. Jensen, F. D'Angelo, D. Turchinovich, M. Bonn, E. Cánovas, Phonon–electron scattering limits free charge mobility in methylammonium lead iodide perovskites. *J. Phys. Chem. Lett.* **6**, 4991–4996 (2015).
67. R. L. Milot, G. E. Eperon, H. J. Snaith, M. B. Johnston, L. M. Herz, Temperature-dependent charge-carrier dynamics in $CH_3NH_3PbI_3$ perovskite thin films. *Adv. Funct. Mater.* **25**, 6218–6227 (2015).
68. H. Oga, A. Saeki, Y. Ogomi, S. Hayase, S. Seki, Improved understanding of the electronic and energetic landscapes of perovskite solar cells : High local charge carrier mobility, reduced recombination, and extremely shallow traps. *J. Am. Chem. Soc.* **136**, 13818–13825 (2014).
69. J. Even, L. Pedesseau, C. Katan, Analysis of multivalley and multibandgap absorption and enhancement of free carriers related to exciton screening in hybrid perovskites. *J. Phys. Chem. C* **118**, 11566–11572 (2014).
70. I. Anusca, S. Balčiūnas, P. Gemeiner, Š. Svirskas, M. Sanlialp, G. Lackner, C. Fettkenhauer, J. Belovickis, V. Samulionis, M. Ivanov, B. Dkhil, J. Banys, V. V. Shvartsman, D. C. Lupascu,

Dielectric response: Answer to many questions in the methylammonium lead halide solar cell absorbers. *Adv. Energy Mater.* **7**, 1700600 (2017).
71. H. Tahara, M. Endo, A. Wakamiya, Y. Kanemitsu, Experimental evidence of localized shallow states in orthorhombic phase of $CH_3NH_3PbI_3$ perovskite thin films revealed by photocurrent beat spectroscopy. *J. Phys. Chem. C* **120**, 5347–5352 (2016).
72. M. E. Ziffer, J. C. Mohammed, D. S. Ginger, Electroabsorption spectroscopy measurements of the exciton binding energy, electron–hole reduced effective mass, and band gap in the perovskite $CH_3NH_3PbI_3$. *ACS Photonics* **3**, 1060–1068 (2016).
73. A. R. Srimath Kandada, S. Neutzner, V. D'Innocenzo, F. Tassone, M. Gandini, Q. A. Akkerman, M. Prato, L. Manna, A. Petrozza, G. Lanzani, Non-linear carrier Interactions in lead halide perovskites and the role of defects. *J. Am. Chem. Soc.* **138**, 13604–13611 (2016).
74. C. G. Bischak, C. L. Hetherington, H. Wu, S. Aloni, D. F. Ogletree, D. T. Limmer, N. S. Ginsberg, Origin of reversible photo-induced phase separation in hybrid perovskites. *Nano Lett.* **17**, 1028–1033 (2017).
75. X. Yang, Y. Wang, H. Li, C. Sheng, Optical properties of heterojunction between hybrid halide perovskite and charge transport materials: Exciplex emission and large polaron. *J. Phys. Chem. C* **120**, 23299–23303 (2016).
76. Y. Zhou, L. You, S. Wang, Z. Ku, H. Fan, D. Schmidt, A. Rusydi, L. Chang, L. Wang, P. Ren, L. Chen, G. Yuan, L. Chen, J. Wang, Giant photostriction in organic–inorganic lead halide perovskites. *Nat. Commun.* **7**, 11193 (2016).
77. J. Gong, M. Yang, X. Ma, R. D. Schaller, G. Liu, L. Kong, Y. Yang, M. C. Beard, M. Lesslie, Y. Dai, B. Huang, K. Zhu, T. Xu, Electron–rotor interaction in organic–inorganic lead iodide perovskites discovered by isotope effects. *J. Phys. Chem. Lett.* **7**, 2879–2887 (2016).
78. M. Kulbak, D. Cahen, G. Hodes, How important is the organic part of lead halide perovskite photovoltaic cells? Efficient $CsPbBr_3$ cells. *J. Phys. Chem. Lett.* **6**, 2452–2456 (2015).
79. H. Zhu, M. T. Trinh, J. Wang, Y. Fu, P. P. Joshi, K. Miyata, S. Jin, X.-Y. Zhu, Organic cations might not be essential to the remarkable properties of band edge carriers in lead halide perovskites. *Adv. Mater.* **29**, 1603072 (2017).
80. L. A. Frolova, D. V. Anokhin, A. A. Piryazev, S. Y. Luchkin, N. N. Dremova, K. J. Stevenson, P. A. Troshin, Highly efficient all-inorganic planar heterojunction perovskite solar cells produced by thermal coevaporation of CsI and PbI_2. *J. Phys. Chem. Lett.* **8**, 67–72 (2017).
81. G. R. Berdiyorov, A. Kachmar, F. El-mellouhi, M. A. Carignano, M. E.-A. Madjet, Role of cations on the electronic transport and optical properties of lead-iodide perovskites. *J. Phys. Chem. C* **120**, 16259–16270 (2016).
82. M. Saliba, T. Matsui, J.-Y. Seo, K. Domanski, J.-P. Correa-Baena, M. K. Nazeeruddin, S. M. Zakeeruddin, W. Tress, A. Abate, A. Hagfeldt, M. Grätzel, Cesium-containing triple cation perovskite solar cells: Improved stability, reproducibility and high efficiency. *Energy Environ. Sci.* **9**, 1989–1997 (2016).
83. D. P. McMeekin, G. Sadoughi, W. Rehman, G. E. Eperon, M. Saliba, M. T. Hörantner, A. Haghighirad, N. Sakai, L. Korte, B. Rech, M. B. Johnston, L. M. Herz, H. J. Snaith, A mixed-cation lead mixed-halide perovskite absorber for tandem solar cells. *Science* **351**, 151–155 (2016).
84. N. Balkan, *Hot Electrons in Semiconductors* (Oxford Univ. Press, 1998).
85. J. Shah, R. F. Leheny, in *Semiconductors Probed by Ultrafast Laser Spectroscopy* (Academic, 1984), p. 45.
86. Z. Guo, Y. Wan, M. Yang, J. Snaider, K. Zhu, L. Huang, Long-range hot-carrier transport in hybrid perovskites visualized by ultrafast microscopy. *Science* **356**, 59–62 (2017).
87. D. M. Monahan, L. Guo, J. Lin, L. Dou, P. Yang, G. R. Fleming, Room-temperature coherent optical phonon in 2D electronic spectra of $CH_3NH_3PbI_3$ perovskite is a possible cooling bottleneck. *J. Phys. Chem. Lett.* **8**, 3211–3215 (2017).
88. T. Ivanovska, C. Dionigi, E. Mosconi, F. De Angelis, F. Liscio, V. Morandi, G. Ruani, Long-lived photoinduced polarons in organohalide perovskites. *J. Phys. Chem. Lett.* **8**, 3081–3086 (2017).
89. J. M. Frost, L. D. Whalley, A. Walsh, Slow cooling of hot polarons in halide perovskite solar cells. arXiv:1708.04158 (2017).
90. A. J. Nozik, Spectroscopy and hot electron relaxation dynamics in semiconductor quantumwells and quantum dots. *Annu. Rev. Phys. Chem.* **52**, 193–231 (2001).
91. U. Bockelmann, G. Bastard, Phonon scattering and energy relaxation in two-, one-, and zero-dimensional electron gases. *Phys. Rev. B.* **42**, 8947–8951 (1990).
92. Y. Yang, D. P. Ostrowski, R. M. France, K. Zhu, J. van de Lagemaat, J. M. Luther, M. C. Beard, Observation of a hot-phonon bottleneck in lead-iodide perovskites. *Nat. Photonics* **10**, 53–59 (2016).
93. M. B. Price, J. Butkus, T. C. Jellicoe, A. Sadhanala, A. Briane, J. E. Halpert, K. Broch, J. M. Hodgkiss, R. H. Friend, F. Deschler, Hot carrier cooling and photo-induced refractive index changes in organic-inorganic lead halide perovskites. *Nat. Commun.* **6**, 8420 (2015).
94. K. Chen, A. J. Barker, F. L. C. Morgan, J. E. Halpert, J. M. Hodgkiss, Effect of carrier thermalization dynamics on light emission and amplification in organometal halide perovskites. *J. Phys. Chem. Lett.* **6**, 153–158 (2015).
95. R. T. Ross, A. J. Nozik, Efficiency of hot-carrier solar energy converters. *J. Appl. Phys.* **53**, 3813–3818 (1982).
96. M. A. Green, *Third Generation Photovoltaics* (Springer, 2006).
97. C. A. Nelson, N. R. Monahan, X.-Y. Zhu, Exceeding the Shockley–Queisser limit in solar energy conversion. *Energy Environ. Sci.* **6**, 3508–3519 (2013).
98. W. Shockley, H. J. Queisser, Detailed balance limit of efficiency of *p-n* junction solar cells. *J. Appl. Phys.* **32**, 510–519 (1961).
99. K. Miyano, N. Tripathi, M. Yanagida, Y. Shirai, Lead halide perovskite photovoltaic as a model *p–i–n* diode. *Acc. Chem. Res.* **49**, 303–310 (2016).
100. A. Walsh, D. O. Scanlon, S. Chen, X. G. Gong, S.-H. Wei, Self-regulation mechanism for charged point defects in hybrid halide perovskites. *Angew. Chem. Int. Ed.* **54**, 1791–1794 (2015).
101. K. X. Steirer, P. Schulz, G. Teeter, V. Stevanovic, M. Yang, K. Zhu, J. J. Berry, Defect tolerance in methylammonium lead triiodide perovskite. *ACS Energy Lett.* **1**, 360–366 (2016).
102. W.-J. Yin, T. Shi, Y. Yan, Unusual defect physics in $CH_3NH_3PbI_3$ perovskite solar cell absorber. *Appl. Phys. Lett.* **104**, 063903 (2014).
103. H. Zhu, Y. Fu, F. Meng, X. Wu, Z. Gong, Q. Ding, M. V. Gustafsson, M. T. Trinh, S. Jin, X.-Y. Zhu, Lead halide perovskite nanowire lasers with low lasing thresholds and high quality factors. *Nat. Mater.* **14**, 636–642 (2015).
104. Y. Fu, H. Zhu, C. C. Stoumpos, Q. Ding, J. Wang, M. G. Kanatzidis, X. Zhu, S. Jin, Broad wavelength tunable robust lasing from single-crystal nanowires of cesium lead halide perovskites ($CsPbX_3$, X= Cl, Br, I). *ACS Nano* **10**, 7963–7972 (2016).
105. Y. Fu, H. Zhu, A. W. Schrader, D. Liang, Q. Ding, P. Joshi, L. Hwang, X.-Y. Zhu, S. Jin, Nanowire lasers of formamidinium lead halide perovskites and their stabilized alloys with improved stability. *Nano Lett.* **16**, 1000–1008 (2016).
106. S. W. Eaton, M. Lai, N. A. Gibson, A. B. Wong, L. Dou, J. Ma, L.-W. Wang, S. R. Leone, P. Yang, Lasing in robust cesium lead halide perovskite nanowires. *Proc. Natl. Acad. Sci. U.S.A.* **113**, 1993–1998 (2016).
107. W. Shockley, W. T. Read Jr., Statistics of the recombinations of holes and electrons. *Phys. Rev.* **87**, 835–842 (1952).
108. R. N. Hall, Electron-hole recombination in germanium. *Phys. Rev.* **87**, 387 (1952).
109. E. J. Juarez-Perez, R. S. Sanchez, L. Badia, G. Garcia-Belmonte, Y. S. Kang, I. Mora-Sero, J. Bisquert, Photoinduced giant dielectric constant in lead halide perovskite solar cells. *J. Phys. Chem. Lett.* **5**, 2390–2394 (2014).
110. A. Walsh, Principles of chemical bonding and band gap engineering in hybrid organic–inorganic halide perovskites. *J. Phys. Chem. C* **119**, 5755–5760 (2015).
111. F. Brivio, A. B. Walker, A. Walsh, Structural and electronic properties of hybrid perovskites for high-efficiency thin-film photovoltaics from first-principles. *APL Mater.* **1**, 042111 (2013).
112. F. Brivio, K. T. Butler, A. Walsh, M. van Schilfgaarde, Relativistic quasiparticle self-consistent electronic structure of hybrid halide perovskite photovoltaic absorbers. *Phys. Rev. B Condens. Matter Mater. Phys.* **89**, 155204 (2014).
113. W.-J. Yin, J.-H. Yang, J. Kang, Y. Yan, S.-H. Wei, Halide perovskite materials for solar cells: A theoretical review. *J. Mater. Chem. A* **3**, 8926–8942 (2015).
114. P. Umari, E. Mosconi, F. De Angelis, Relativistic GW calculations on $CH_3NH_3PbI_3$ and $CH_3NH_3SnI_3$ perovskites for solar cell applications. *Sci. Rep.* **4**, 4467 (2014).
115. A. Miyata, A. Mitioglu, P. Plochocka, O. Portugall, J. T.-W. Wang, S. D. Stranks, H. J. Snaith, R. J. Nicholas, Direct measurement of the exciton binding energy and effective masses for charge carriers in organic–inorganic tri-halide perovskites. *Nat. Phys.* **11**, 582–587 (2015).
116. J. Bardeen, W. Shockley, Deformation potentials and mobilities in non-polar crystals. *Phys. Rev.* **80**, 72–80 (1950).
117. T. Zhao, W. Shi, J. Xi, D. Wang, Z. Shuai, Intrinsic and extrinsic charge transport in $CH_3NH_3PbI_3$ perovskites predicted from first-principles. *Sci. Rep.* **7**, 19968 (2016).
118. Y. Wang, Y. Zhang, P. Zhang, W. Zhang, High intrinsic carrier mobility and photon absorption in the perovskite $CH_3NH_3PbI_3$. *Phys. Chem. Chem. Phys.* **17**, 11516–11520 (2015).
119. P.-A. Mante, C. C. Stoumpos, M. G. Kanatzidis, A. Yartsev, Electron–acoustic phonon coupling in single crystal $CH_3NH_3PbI_3$ perovskites revealed by coherent acoustic phonons. *Nat. Commun.* **8**, 14398 (2017).
120. A. Filippetti, A. Mattoni, C. Caddeo, M. I. Saba, P. Delugas, Low electron-polar optical phonon scattering at the fundament of carrier mobility in methylammonium lead halide $CH_3NH_3PbI_3$ perovskites. *Phys. Chem. Chem. Phys.* **18**, 15352–15362 (2016).
121. A. D. Wright, C. Verdi, R. L. Milot, G. E. Eperon, M. A. Pérez-Osorio, H. J. Snaith, F. Giustino, M. B. Johnston, L. M. Herz, Electron–phonon coupling in hybrid lead halide perovskites. *Nat. Commun.* **7**, 11755 (2016).
122. A. J. Neukirch, W. Nie, J.-C. Blancon, K. Appavoo, H. Tsai, M. Y. Sfeir, C. Katan, L. Pedesseau, J. Even, J. J. Crochet, G. Gupta, A. D. Mohite, S. Tretiak, Polaron stabilization by cooperative lattice distortion and cation rotations in hybrid perovskite materials. *Nano Lett.* **16**, 3809–3816 (2016).

123. Y. Ōsaka, Polaron state at a finite temperature. *Prog. Theor. Phys.* **22**, 437–446 (1959).
124. J. M. Frost, Calculating polaron mobility in halide perovskites. arXiv:1704.05404 (2017).
125. M. I. Saidaminov, A. L. Abdelhady, B. Murali, E. Alarousu, V. M. Burlakov, W. Peng, I. Dursun, L. Wang, Y. He, G. Maculan, A. Goriely, T. Wu, O. F. Mohammed, O. M. Bakr, High-quality bulk hybrid perovskite single crystals within minutes by inverse temperature crystallization. *Nat. Commun.* **6**, 7586 (2015).
126. R. Zwanzig, Dielectric friction on a rotating dipole. *J. Chem. Phys.* **38**, 1605–1606 (1963).
127. M. B. Johnston, L. M. Herz, Hybrid perovskites for photovoltaics: Charge-carrier recombination, diffusion and radiative efficiencies. *Acc. Chem. Res.* **49**, 146–154 (2016).
128. P. Langevin, Recombinaison et mobilites des ions dans les gaz. *Ann. Chim. Phys.* **28**, 433–530 (1903).
129. M. Pope, C. E. Swenberg, *Electronic Processes in Organic Crystals and Polymers* (Oxford Univ. Press, 1999).
130. F. Zheng, L. Z. Tan, S. Liu, A. M. Rappe, Rashba spin–orbit coupling enhanced carrier lifetime in $CH_3NH_3PbI_3$. *Nano Lett.* **15**, 7794–7800 (2015).
131. M. Kepenekian, R. Robles, C. Katan, D. Sapori, L. Pedesseau, J. Even, Rashba and dresselhaus effects in hybrid organic–inorganic perovskites: From basics to devices. *ACS Nano* **9**, 11557–11567 (2015).
132. T. Etienne, E. Mosconi, F. De Angelis, Dynamical origin of the rashba effect in organohalide lead perovskites: A key to suppressed carrier recombination in perovskite solar cells? *J. Phys. Chem. Lett.* **7**, 1638–1645 (2016).
133. D. Niesner, M. Wilhelm, I. Levchuk, A. Osvet, S. Shrestha, M. Batentschuk, C. Brabec, T. Fauster, Giant rashba splitting in $CH_3NH_3PbBr_3$ organic-inorganic perovskite. *Phys. Rev. Lett.* **117**, 126401 (2016).
134. J. Ma, L.-W. Wang, Nanoscale charge localization induced by random orientations of organic molecules in hybrid perovskite $CH_3NH_3PbI_3$. *Nano Lett.* **15**, 248–253 (2015).
135. E. M. Hutter, M. C. Gélvez-Rueda, A. Osherov, V. Bulović, F. C. Grozema, S. D. Stranks, T. J. Savenije, Direct–indirect character of the bandgap in methylammonium lead iodide perovskite. *Nat. Mater.* **16**, 115–120 (2017).
136. T. Wang, B. Daiber, J. M. Frost, S. A. Mann, E. C. Garnett, A. Walsh, B. Ehrler, Indirect to direct bandgap transition in methylammonium lead halide perovskite. *Energy Environ. Sci.* **10**, 509–515 (2017).
137. T. Kirchartz, U. Rau, Decreasing radiative recombination coefficients via an indirect band gap in lead halide perovskites. *J. Phys. Chem. Lett.* **8**, 1265–1271 (2017).
138. W. van Roosbroeck, W. Shockley, Photon-radiative recombination of electrons and holes in germanium. *Phys. Rev.* **94**, 1558–1560 (1954).
139. J. I. Pankove, *Optical Processes in Semiconductors* (Courier Corporation, 2012).
140. X. Wu, M. T. Trinh, D. Niesner, H. Zhu, Z. Norman, J. S. Owen, O. Yaffe, B. J. Kudisch, X.-Y. Zhu, Trap states in lead iodide perovskites. *J. Am. Chem. Soc.* **137**, 2089–2096 (2015).
141. M. Saba, F. Quochi, A. Mura, G. Bongiovanni, Excited state properties of hybrid perovskites. *Acc. Chem. Res.* **49**, 166–173 (2016).
142. Y. Yang, M. Yang, K. Zhu, J. C. Johnson, J. J. Berry, J. van de Lagemaat, M. C. Beard, Large polarization-dependent exciton optical Stark effect in lead iodide perovskites. *Nat. Commun.* **7**, 12613 (2016).
143. S. Nah, B. Spokoyny, C. Stoumpos, C. M. M. Soe, M. Kanatzidis, E. Harel, Spatially segregated free-carrier and exciton populations in individual lead halide perovskite grains. *Nat. Photonics* **11**, 285–288 (2017).

Acknowledgments: X.-Y.Z. thanks V. Podzorov, S. Jin, and F. De Angelis for fruitful collaborations; X. Roy, M. Bonn, A. Walsh, and J. Frost for insightful discussions; and D. Niesner, X. Wu, H. Zhu, M. Tuan Trinh, J. Wang, and P. Joshi for the experimental work, which precipitated the ideas presented here. **Funding:** X.-Y.Z. acknowledges the NSF (grant DMR 1420634) (Materials Research Science and Engineering Center) for support during the writing of this perspective. The experimental works presented in Figs. 3 and 6 to 9 were supported by the U.S. Department of Energy, Office of Science, Basic Energy Sciences (grant ER46980). K.M. acknowledges the financial support of the Japan Society for the Promotion of Science. **Author contributions:** K.M., T.L.A., and X.-Y.Z. contributed to the reviewing of literature and writing of this perspective. **Competing interests:** The authors declare that they have no competing interests. **Data and materials availability:** All data needed to evaluate the conclusions in the paper are present in the paper. Additional data related to this paper may be requested from the authors.

Submitted 4 May 2017
Accepted 14 September 2017
Published 13 October 2017
10.1126/sciadv.1701469

Citation: K. Miyata, T. L. Atallah, X.-Y. Zhu, Lead halide perovskites: Crystal-liquid duality, phonon glass electron crystals, and large polaron formation. *Sci. Adv.* **3**, e1701469 (2017).